

Supplementary Information for:

Brittle-layer-tuned Microcrack Propagation for High-performance Stretchable Strain Sensors

Fei Han,^{abc} Rui Su,^b Lijun Teng,^b Ruijie Xie,^b Qianhengyuan Yu,^b Qingsong Li,^b Qiong Tian,^b Hanfei Li,^b Jing Sun,^b Yuan Zhang,^d Min Li,^a Xu Liu,^c Huaiyu Ye,^c Guanglin Li,^b Guoqi Zhang^{*ac} and Zhiyuan Liu^{*b}

^a. Institute of Future Lighting, Academy for Engineering and Technology, Fudan University, Shanghai 200433, China.

^b. Neural Engineering Centre, Shenzhen Institute of Advanced Technology, Chinese Academy of Sciences, Shenzhen 518055, China.

^c. Shenzhen Institute of Wide-Bandgap Semiconductors, Shenzhen 518055, China.

^d. Department of Materials Science and Engineering, Southern University of Science and Technology, Shenzhen 518055, China.

* Corresponding Authors: zy.liu1@siat.ac.cn; G.Q.Zhang@tudelft.nl

Contents:

Fig. S1. Fabrication process of the stretchable strain sensor, images of the prepared sensors, SEM characterization of original PDMS, 1 min, 10 min and 20min plasma treatment at 300 W power, (P-1, P-10 and P-20), cracks distribution of P-1, P-10 and P-20 samples.

Fig. S2. Mechanical property curves, cross-sectional images of brittle layer, SEM characterization of 30, 60, 100 cycled pre-crazing samples (P-30c, P-60c and P-100c sample, respectively).

Fig. S3. XPS characterization of PDMS substrate before and after oxygen plasma treatment.

Fig. S4. The surface morphology variation of P-0c and P-30c during stretching process.

Fig. S5. The surface morphology variation of P-100c during stretching process.

Fig. S6. Performance of Au decorated samples, and SEM characterization of those stretchable strain sensors during stretching process.

Fig. S7. Comparison of sensing performance in terms of gauge factor and linear sensing range of strain sensors in this work with the recently reported works in literatures.

Fig. S8. Performance enlarged view of sample P-1, P-10 and P-20 within 40% strain, GF values summarizing of P-1, P-10 and P-20 samples in divided strain section, and two attachable applications.

Fig. S9. Surface topography variation of sample P-1, P-10 and P-20 samples during stretching process.

Fig. S10. XPS characterization of Ecoflex substrate before and after plasma treatment.

Fig. S11. SEM characterization of Ecoflex substrate based stretchable strain sensors during stretching process.

Fig. S12 The encapsulation structure and packaged sensor images.

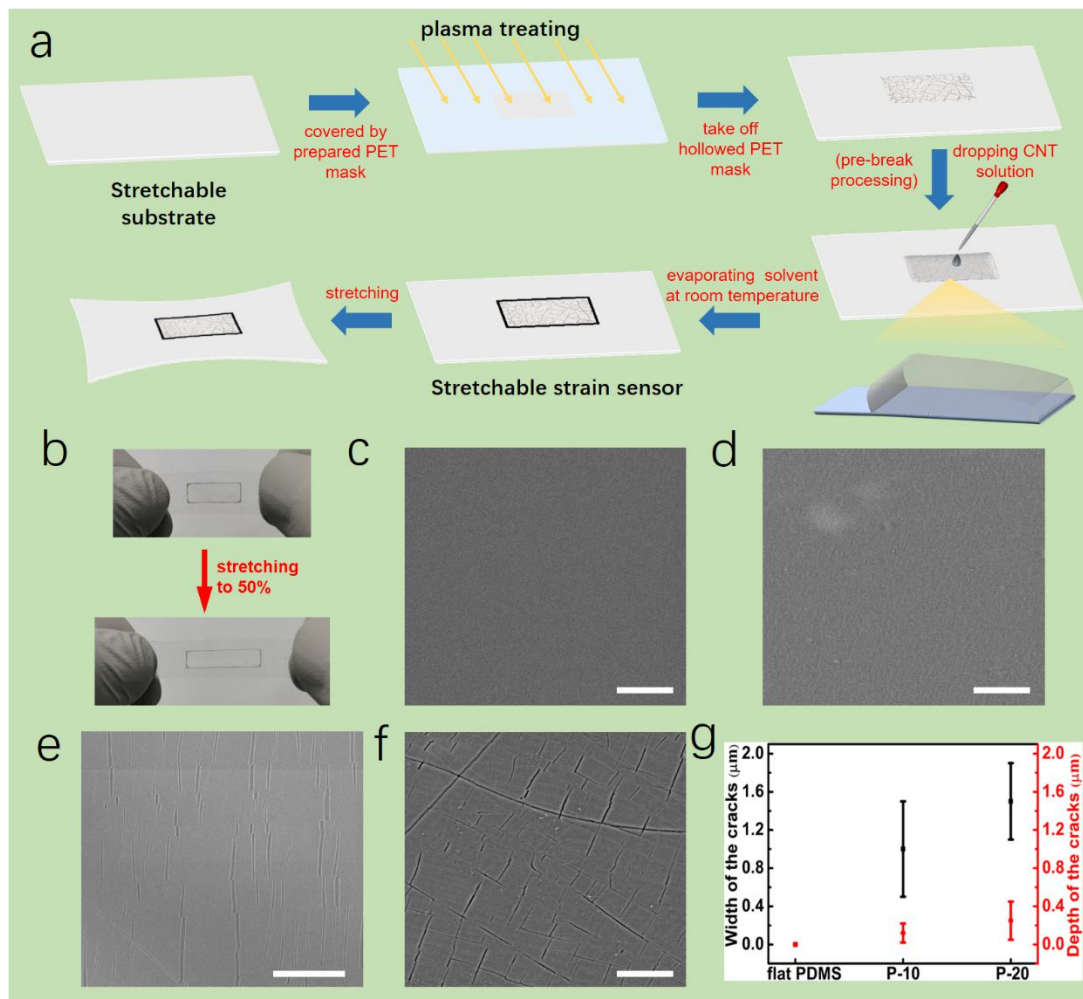


Fig. S1 (a) A schematic of the fabrication process of the brittle silica layer based stretchable strain sensor. (b) Images of the fabricated strain sensor and stretch to 50% strain. (c-f) SEM surface image of original PDMS, P-1, P-10 and P-20 samples. Scale bar, 20 μm . (g) Width and depth distribution of the cracks on the surface of sample P-1, P-10 and P-20.

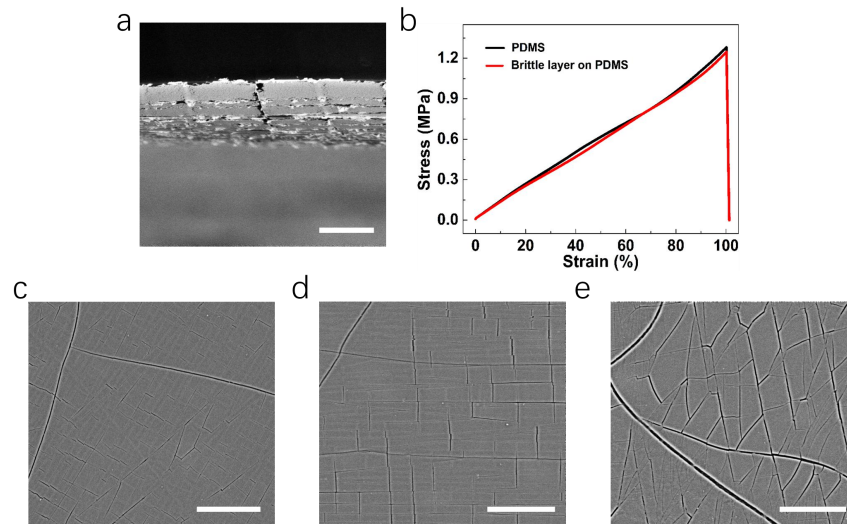


Fig. S2 (a) The cross-section of brittle layer on PDMS substrate. Scale bar, 1 μm . (b) The stress-strain curves for PDMS substrate and brittle layer decorated PDMS. (b-d) Surface topography of P-30c, P-60c and P-100c sample, respectively. Scale bar, 30 μm .

Fig. S2a-e reveals the multi-layer structure of brittle layer and pre-crazing treatment resulted more rougher surface of those samples, including increased cracks width and depth.

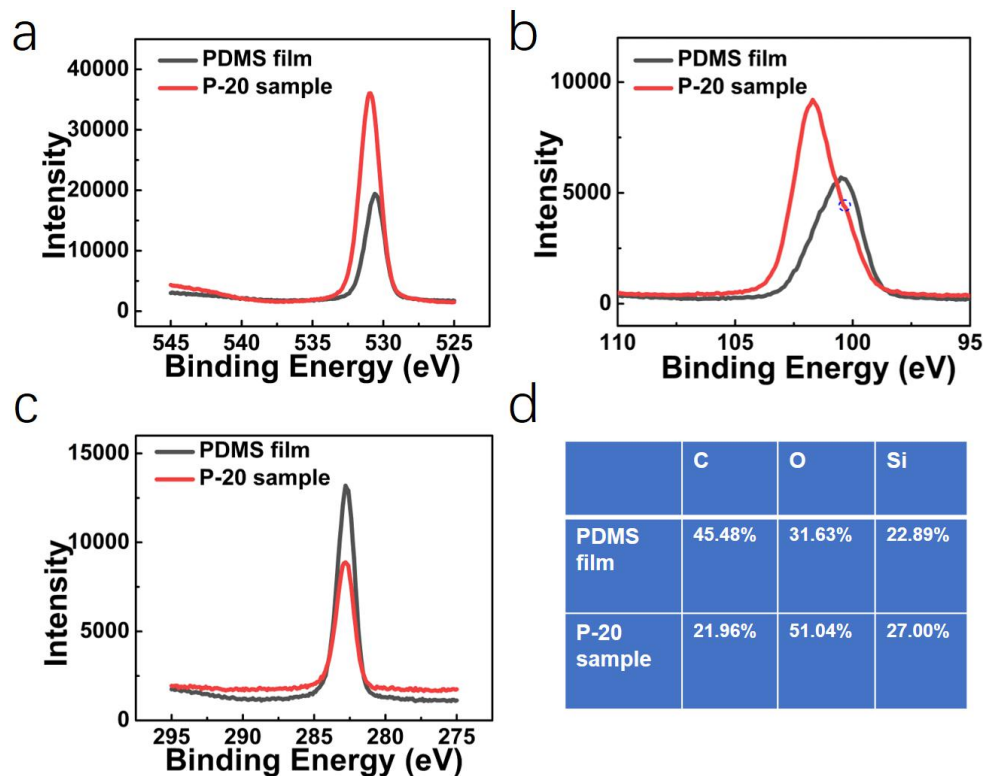


Fig. S3 (a) XPS O 1s region of PDMS film and P-20 sample. (b) XPS Si 2p region of PDMS film and P-20 sample. (c) XPS C 1s region of PDMS film and P-20 sample. (d) XPS surface element analysis of PDMS film and P-20 sample.

Fig. S3a-c shows the high-resolution spectra in the O 1s, Si 2p and C 1s regions of PDMS film and P-20 sample, respectively. It can be seen from the figure that the Si 2p peak and O 1s peak of the treated PDMS are obviously wider and the intensity of the peaks is also larger. It is obvious that there is one more peak at 101.6eV for Si 2p, which indicates the change of chemical state of Si. The position of Si 2p and O 1s peaks of PDMS after treatment shifted to the left. Both the peak value and peak width of C 1s in the P-20 sample are decrease. According to the element analysis in Fig. S3d, the content of carbon decreases and the ratio of oxygen and silicon increases, which confirms the formation of SiO_x . And the formatted SiO_x thin layer remains good adhesion with the PDMS film substrate, which is vital for the relative stability of cracks extension and propagation during the stretching process. Not only cracks generated on the PDMS surface, but also the hydrophilic was strengthened.

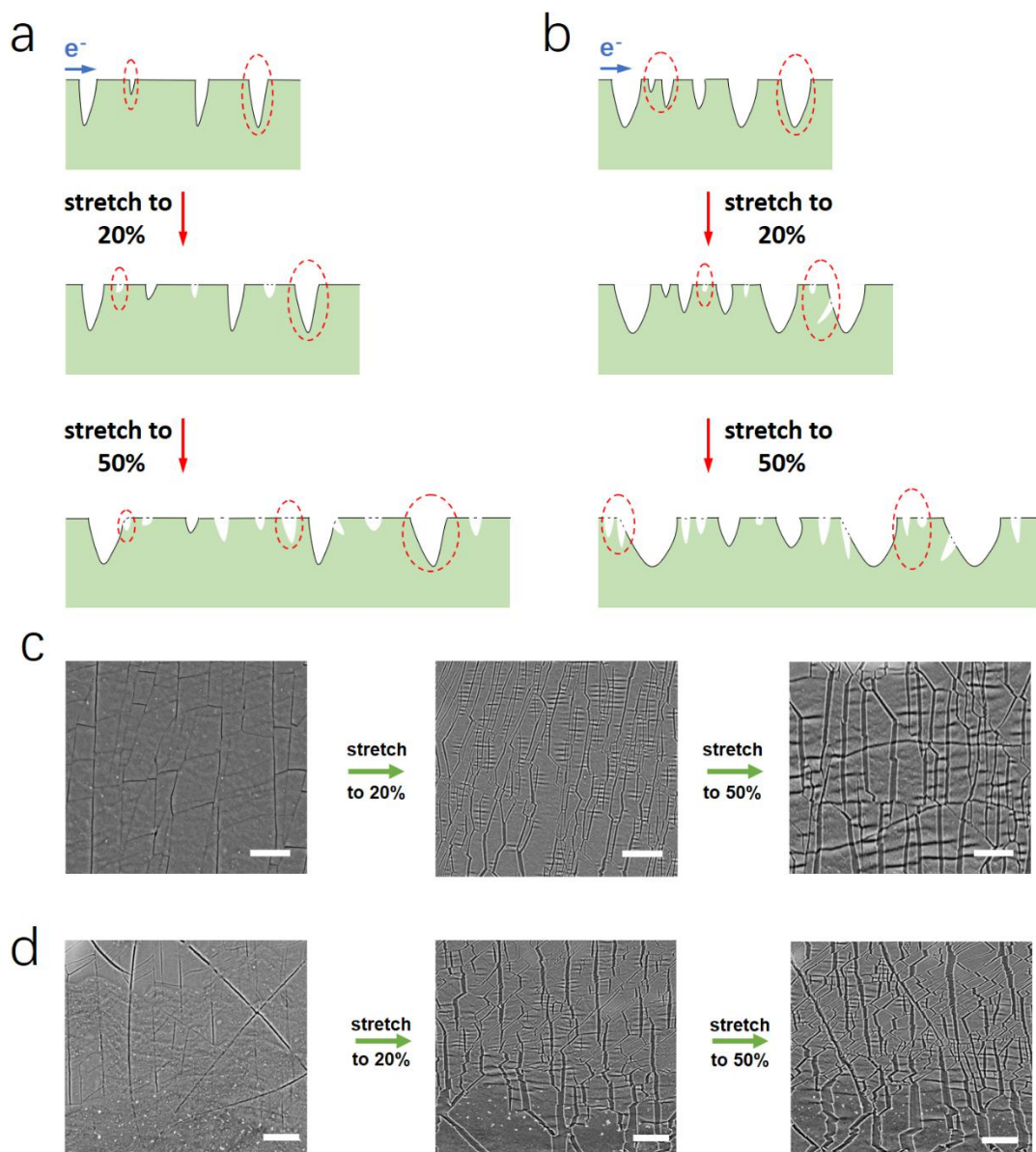


Fig. S4 (a-b) Schematic diagram of the structure variation of P-0c and P-30c under 0%→20%→50% strain, respectively. (c-d) SEM characterization of P-0c and P-30c variation respectively corresponding to strain process in figure a and b. Scale bar, 30 μm .

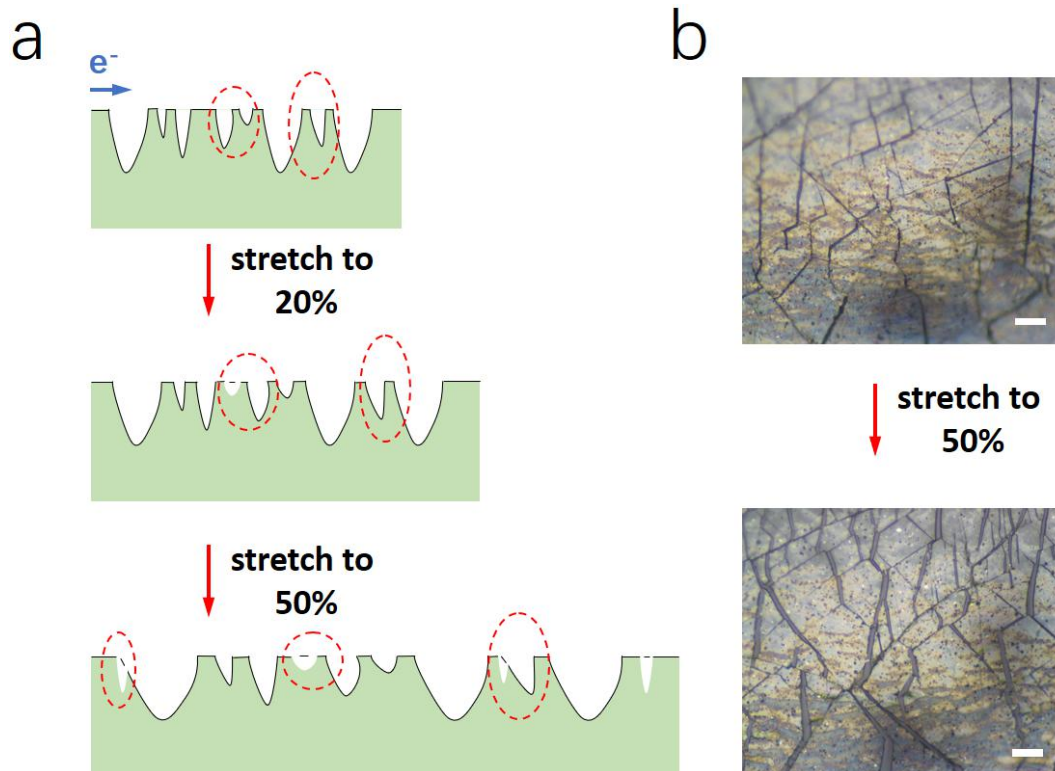


Fig. S5 (a) Schematic diagram of the structure variation of P-100c under 0%→20%→50% strain. (b) Optical micrographs images of P-100c when stretched to 50% strain. Scale bar, 10 μm .

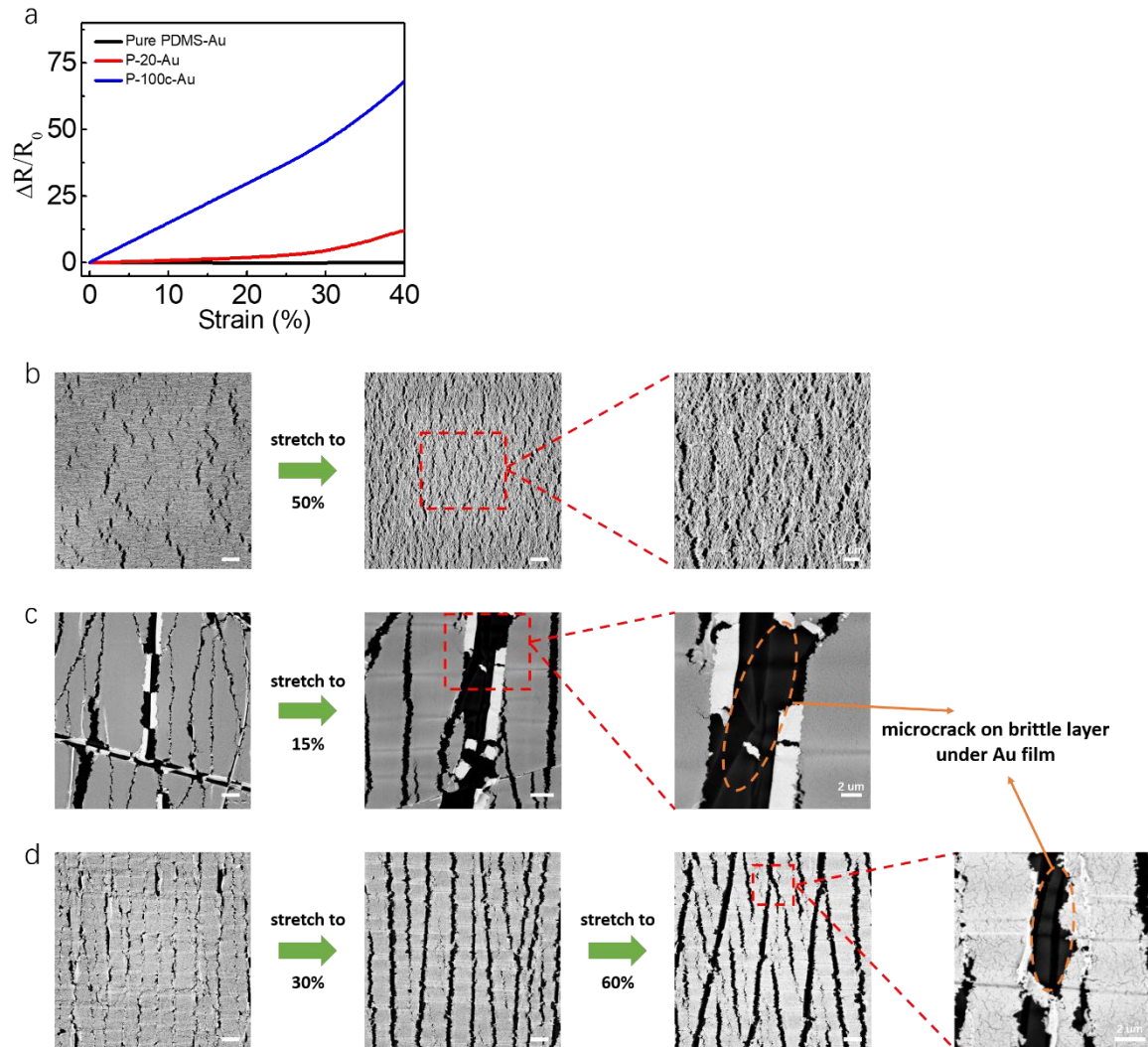


Fig. S6 (a) The enlarged view within 40% strain for relative resistance changes of Au film decorated samples (Au decorated pure PDMS film (Pure PDMS-Au), 20 min oxygen plasma treated PDMS film with Au decorating (P-20-Au), 20 min plasma treated PDMS film with 100 cycles pre-crazing process and Au decorating (P-100c-Au)). (b-d) The surface morphology variation of sample Pure PDMS-Au, P-20-Au and P-100c-Au under different strain. Scale bar, 5 μm .

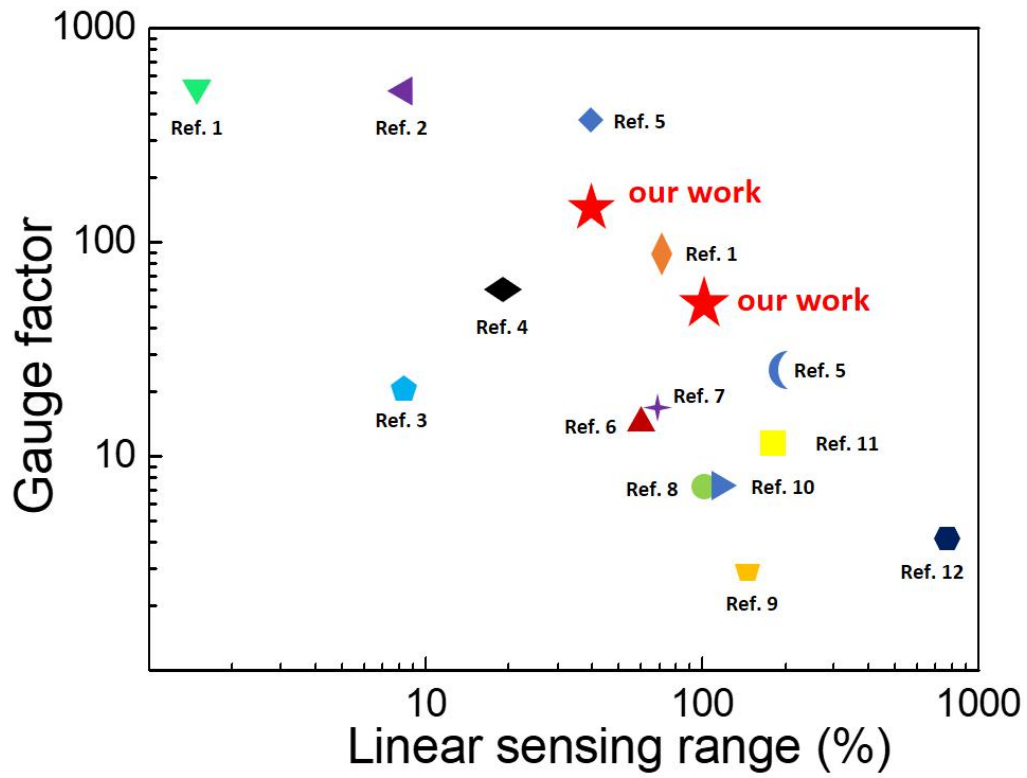


Fig. S7 Comparison of sensing performance in terms of gauge factor and linear sensing range of strain sensors in this work with the recently reported works in literatures.

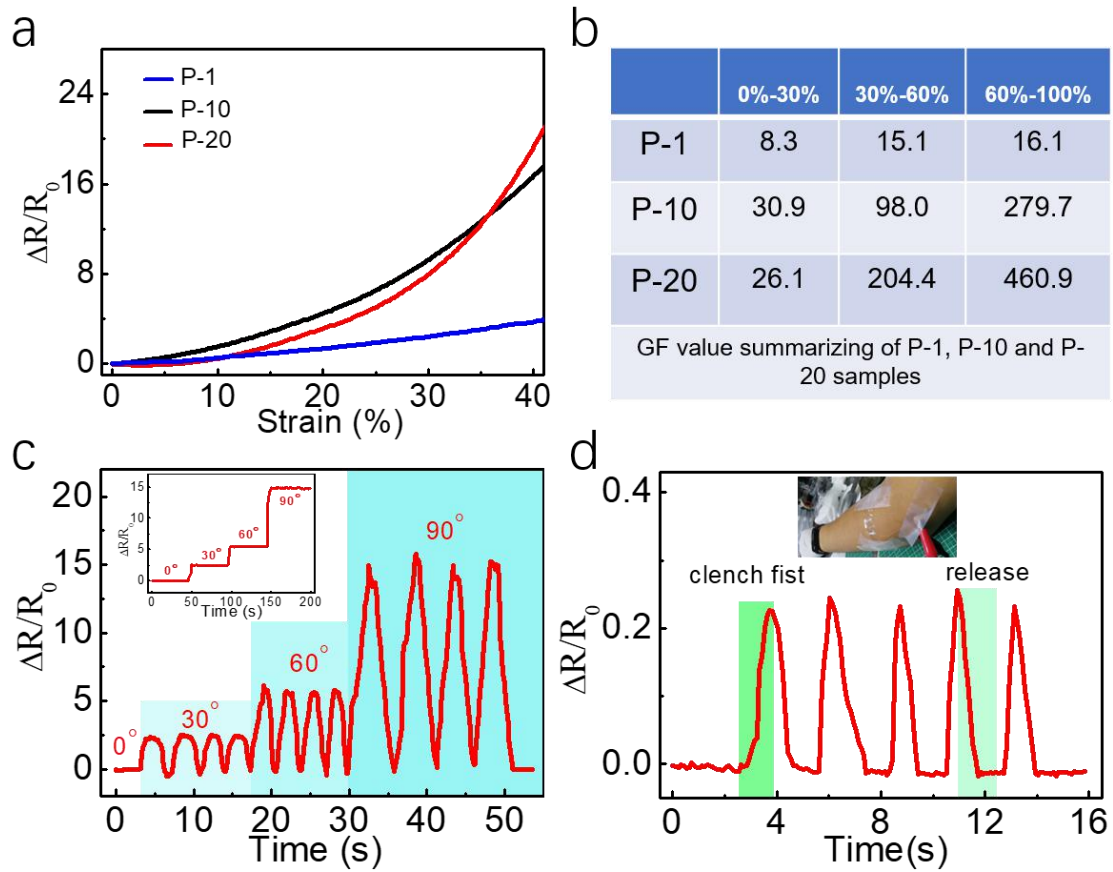


Fig. S8 (a) Relative resistance change of sample P-1, P-10 and P-20 within 40% strain, enlarged view of Fig. 4a. (b) GF value summarizing of sample P-1, P-10 and P-20 in different strain section. (c) Monitoring signals when the sensor attached to human finger at different bending angles. (d) The signals when monitoring the contraction and relaxation of brachioradialis muscle triggered by clenched and unclenched fist.

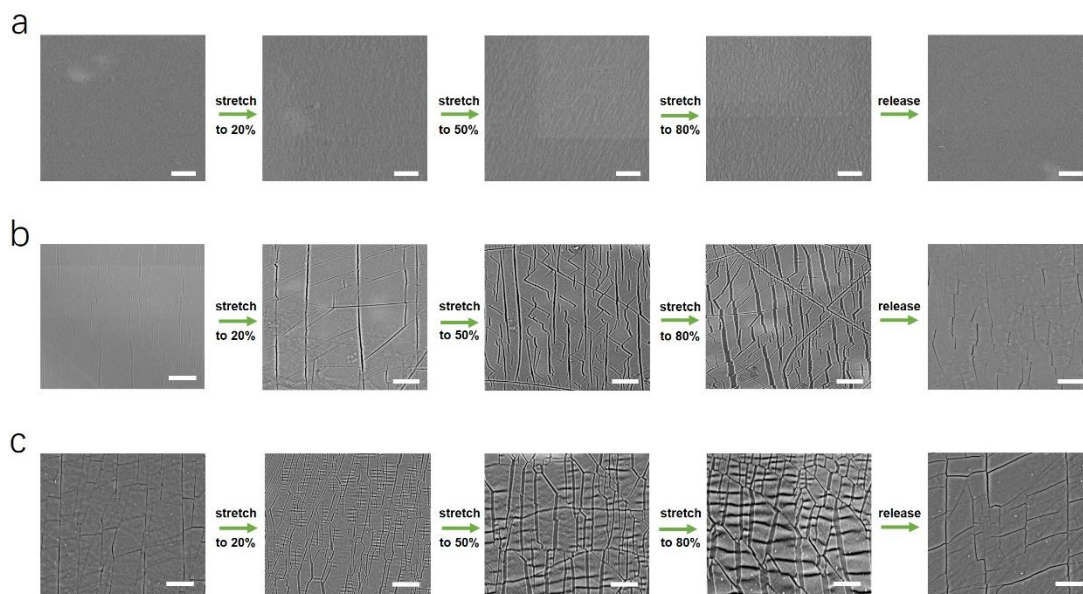


Fig. S9 (a) SEM images of sample P-1 during stretch process (20%, 50%, 80%). scale bar, 20 μm . (b) SEM images of sample P-10 during stretch process (20%, 50%, 80%). scale bar, 20 μm . (c) SEM images of sample P-20 during stretch process (20%, 50%, 80%). scale bar, 30 μm .

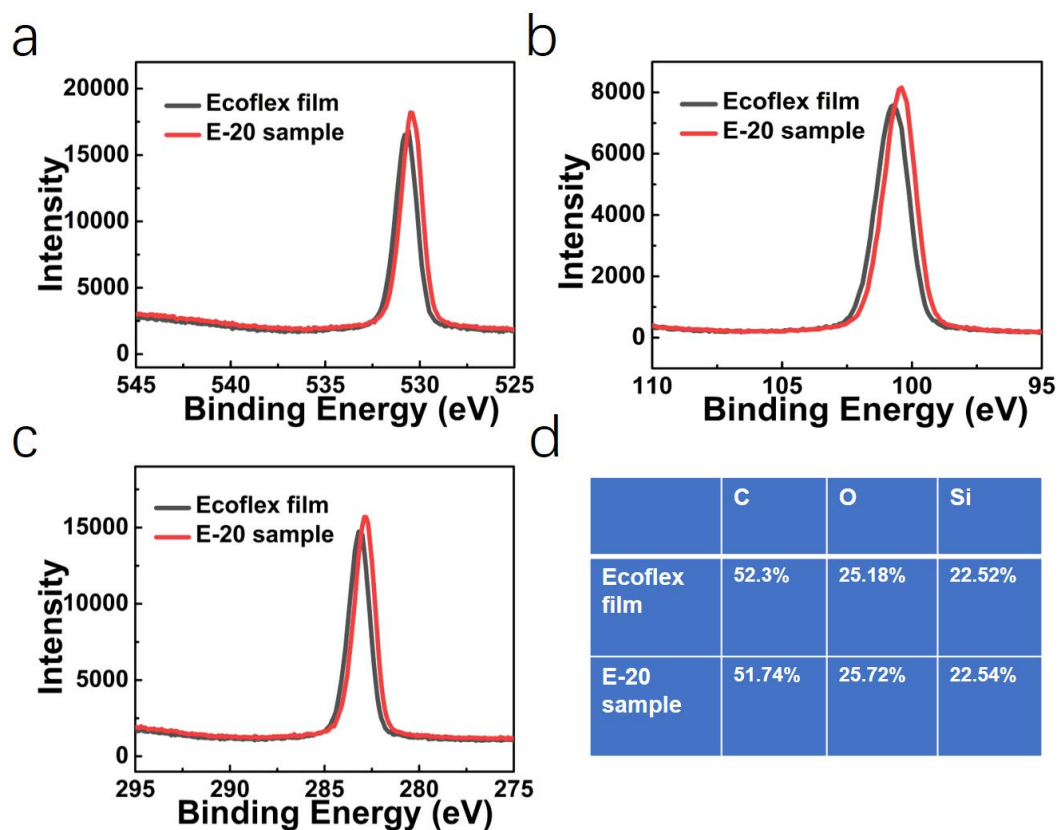


Fig. S10 (a) XPS O 1s region of Ecoflex film and E-20 sample. (b) XPS Si 2p region of Ecoflex film and E-20 sample. (c) XPS C 1s region of Ecoflex film and E-20 sample. (d) XPS surface element analysis of Ecoflex film and E-20 sample.

Through XPS characterization for Ecoflex substrate before and after plasma treatment (Fig. S7a-c), it can be seen that the O 1s peak, Si 2p peak and C1s peak of the treated Ecoflex slightly move to the right. It is obvious that the sample after treatment has a stronger peak value. However, according to the element analysis, the proportion of the three elements did not change significantly, indicating the generating of brittle layer differently from that on PDMS substrate.

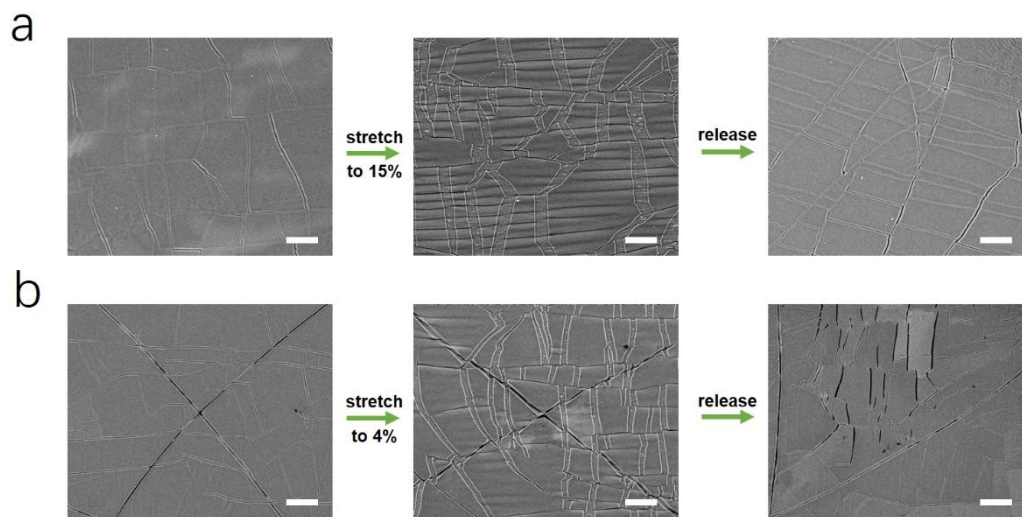


Fig. S11 SEM characterization of Ecoflex substrate based stretchable strain sensor (a) E-10 and (b) E-20 during stretch and release phases. Scale bar, 50 μm and 100 μm , respectively.

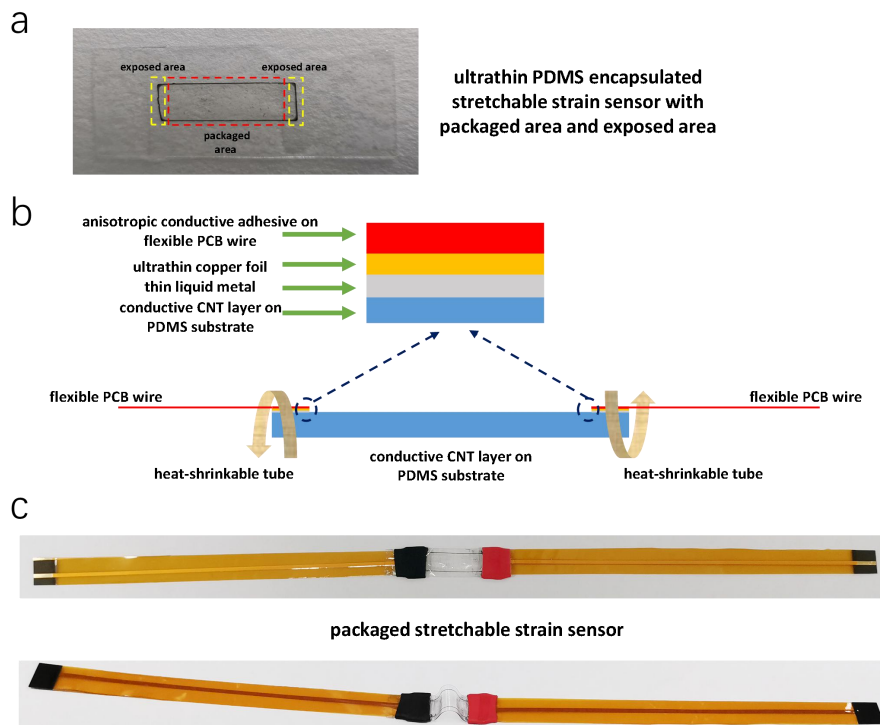


Fig. S12 (a) Ultrathin PDMS encapsulated stretchable strain sensor with packaged area and exposed area by high speed spinning coating technology. (b) The structure of packaged strain sensor by using liquid metal, copper foil, anisotropic conductive adhesive on flexible PCB wire and heat-shrinkable tube. (c) The images of packaged stretchable strain sensor.

A thin PDMS film was fabricated as the encapsulation layer by directly spinning coating with speed of 3000 rpm. It exhibited good light transmittance and successfully integrated with the sensing part (Fig. S12a). The wire-bonding area was exposed by beforehand covering a removable shielding layer which was removed immediately after the spin coating. Then, flexible PCBs were employed as the interconnector for further testing. The integrated structure of the interconnecting area is shown in Fig. S12b. In detail, a thin liquid metal was firstly dropped in the exposed area. Then, a copper foil layer was attached to the ultrathin liquid metal layer. After pressing the flexible PCB with an anisotropic conductive adhesive onto the copper foil, the heat-shrinkable tube was employed to fix and protect the connection joint. And the image of the packaged sensor is shown in Fig. S12c.

Reference

- 1 J. Zhao, C. He, R. Yang, Z. Shi, M. Cheng, W. Yang, G. Xie, D. Wang, D. Shi and G. Zhang, *Appl. Phys. Lett.*, 2012, **101**, 063112.
- 2 T. Yang, W. Wang, H. Zhang, X. Li, J. Shi, Y. He, Q. Zheng, Z. Li and H. Zhu, *ACS Nano*, 2015, **9**, 10867–10875.
- 3 Q. Liu, M. Zhang, L. Huang, Y. Li, J. Chen, C. Li and G. Shi, *ACS Nano*, 2015, **9**, 12320–12326.
- 4 S. Wu, R. B. Ladani, J. Zhang, K. Ghorbani, X. Zhang, A. P. Mouritz, A. J. Kinloch and C. H. Wang, *ACS Appl. Mater. Interfaces*, 2016, **8**, 24853–24861.
- 5 S. Peng, S. Wu, Y. Yu, P. Blanloeuil, C. Wang, *J. Mater. Chem. A*, 2020, **8**, 20531–20542
- 6 Y. R. Jeong, H. Park, S. W. Jin, S. Y. Hong, S.-S. Lee and J. S. Ha, *Adv. Funct. Mater.*, 2015, **25**, 4228–4236.
- 7 Q. Liu, J. Chen, Y. Li and G. Shi, *ACS Nano*, 2016, **10**, 7901–7906.
- 8 C. Yan, J. Wang, W. Kang, M. Cui, X. Wang, C. Y. Foo, K. J. Chee and P. S. Lee, *Adv. Mater.*, 2014, **26**, 2022–2027.
- 9 J. J. Park, W. J. Hyun, S. C. Mun, Y. T. Park and O. O. Park, *ACS Appl. Mater. Interfaces*, 2015, **7**, 6317–6324.
- 10 Z. Zeng, S. I. Seyed Shahabadi, B. Che, Y. Zhang, C. Zhao and X. Lu, *Nanoscale*, 2017, **9**, 17396–17404.
- 11 P. Wang, W. Wei, Z. Li, W. Duan, H. Han and Q. Xie, *J. Mater. Chem. A*, 2020, **8**, 3509–3516.
- 12 L. M. Zhang, Y. He, S. Cheng, H. Sheng, K. Dai, W. J. Zheng, M. X. Wang, Z. S. Chen, Y. M. Chen and Z. Suo, *Small*, 2019, **15**, 1804651.